Proceedings of the 7th International Symposium on Cavitation
CAV2009 - Paper No. 89
August 17-22, 2009, Ann Arbor, Michigan, USA

Investigation of Turbulent Modulation by Cavitation for Subgrid-scale Modeling in LES

Kie OKABAYASHI
Osaka University Graduate School,
JSPS Research Fellow
Suita, Osaka, Japan

Takeo KAJISHIMA
Osaka University
Suita, Osaka, Japan

ABSTRACT

The two-way interaction between cavitation and turbulence was investigated by the direct numerical simulation of a spatially-developing mixing layer. Namely, the vortical structure and Reynolds stress components were compared between cavitating and non-cavitating conditions. Under cavitating condition, cavitation mainly occur in the regions of low pressure which are corresponding to vortices. Under cavitating condition, instability of mixing layer is caused more easily due to disturbance by cavitation to the flow field. Therefore, cavitation excites the instability of shear layer: vortices generating and pairing. As a result of stimulated pairing, the pitch of roll-cell vortices become longer than that in non-cavitating condition. One of the circumferential components of roll-cell vortices is suppressed by the decreasing of the number of roll-cell vortices. Circumferential component of streamwise vortices, on the other hand, tends to increase in comparison with non-cavitating condition. This is explained by volume fluctuation by cavitation. The modulation of Reynolds stress is consistently described by these changes in vortical stractures.

INTRODUCTION

Flows in hydro-machineries are affected by various types of cavitation, and most of them are in turbulence. To simulate cavitating turbulent flows, a variety of methods have been developed. Most of them adopt RANS to deal with turbulence [1–3]. This practical method, however, is model-dependent, so it is not useful for understanding of interaction between turbulence and cavitation. Beside, numerical method with RANS is time-averaged, so large-scale unsteadiness in cavitating flow field cannot be considered. On the other hand, LES or DES has become available for unsteady cavitating flows [4–7]. These methods, however, have not taken account of cavitation which occurs in fine-scale elementary vortices, because they are mostly in subgrid scale (SGS). This could reduce the accuracy in predicting turbulent modulation by cavitation as well as cavitation inception [8]. From this view point, we aim at development of cavitation LES model which takes into account cavitation in elementary vortices.

We are going to model the modulation in kinetic energy and dissipation rate of SGS elementary vortices corresponding to cavitation inception or contraction. In this study, we investigate interaction between cavitation and turbulence for LES modeling. We select spatially-developing turbulent mixing layer as the flow field. Mixing layer is a typical free turbulence and there are a lot of theoretical, experimental and numerical investigation for single phase flow. Reducing the cavitation number, interaction between cavitation and typical free turbulence is observed.

OUTLINE OF COMPUTATION

The procedure including cavitation model and numerical method should be suitable for the spatio-temporal scale of unsteady motion of vortices in the turbulent shear layer. In this study, we apply the method developed by Okita and Kajishima [9].

Governing Equation

Hereafter, all variables are non-dimensionalized by a characteristic length H, velocity u_∞, and the liquid density $\rho_{L\infty}$ at sufficiently far position. The flow field is assumed to be isothermal. A low-Mach number assumption is applied considering the weak compressibility of liquid [10].

The governing equations are the conservation laws of mass and momentum of homogeneous mixture of liquid and cavity:

$$\frac{Df_L}{Dt} + f_L\left(M^2\frac{Dp}{Dt} + \frac{\partial u_i}{\partial x_i}\right) = 0 \tag{1}$$

$$\frac{\partial u_i}{\partial t} + u_j\frac{\partial u_i}{\partial x_j} = -\frac{1}{f_L}\frac{\partial p}{\partial x_i} + \frac{1}{Re}\frac{\partial^2 u_i}{\partial x_j \partial x_j} \tag{2}$$

where u_i is the velocity component, p the pressure, and f_L the volumetric fraction of liquid. A Mach number $M(=u_\infty/c,\ c$ the sound speed) is given uniformly in a computational domain.

Cavitation Model

In the present study, we used following cavitation model

$$\frac{Df_L}{Dt} = \left[C_g(1-f_L) + C_l f_L\right](p - p_v). \tag{3}$$

This model is a modification of Chen's model [11], which is based on the analytic consideration of Rayleigh-Plesset equation. This equation simply means that cavitation region will expand when pressure p is lower than saturated vapor pressure p_v, whereas it will contract when p is higher than p_v. The model constants are $C_g = 100$ and $C_l = 1$. Kajishima et al. [12] refer some details of derivation of this model.

The saturated vapor pressure p_v is given by

$$\sigma = \frac{p_\infty - p_v}{\frac{1}{2}\rho_L u_\infty^2}, \tag{4}$$

where p_∞ and $\rho_{L\infty}$ is the pressure and liquid density at far distance.

Numerical Methods

The method of unsteady numerical simulation is based on the fractional step method for incompressible flow. The convective term and viscous term are discretised by central finite difference of 2nd order accuracy. Adams-Bashforth method of 2nd order accuracy is applied for time marching of these terms.

The pressure equation

$$\frac{Df_L}{Dt} + f_L\left\{M^2\left(\frac{\partial p}{\partial t} + u_j\frac{\partial p}{\partial x_j}\right) + \frac{\partial \tilde{u}_j}{\partial x_j} - \Delta t\frac{\partial}{\partial x_j}\left(\frac{1}{f_L}\frac{\partial p}{\partial x_j}\right)\right\} = 0 \tag{5}$$

where $\tilde{u}_j$ is fractional step and is derived from equation 1, is discretized using 3-step method for time difference and 2nd order central difference for space. Eq. 5 is converged by the relaxation method. Then using the pressure calculated from above procedure, the velocity at next step is directed by adding the pressure gradient to the fractional step and time marching is completed. Time marching for liquid volumetric fraction f_L is semi-implicit scheme and conducted for two-stage. Readers can find a detail of our numerical method in Okita and Kajishima [9].

Computational Conditions

The flow field is a spatially-developing turbulent mixing layer as shown in Figure 1. The height H is selected for the length scale. The size of the domain is $H_x = 10H$ in the mainstream direction and $H_z = H$ in the spanwise direction. The periodicity is assumed in the spanwise direction. In this computation, velocity ratio U_1/U_2 is 2. The mean velocity difference $\Delta U = U_1 - U_2$ is used for the velocity scale. In a mixing layer, primary roll-cell vortices are generated due to Kelvin-Helmholtz instability. In the stretched region between two neighboring vortices, streamwise (rib) vortices are caused by the secondary instability.

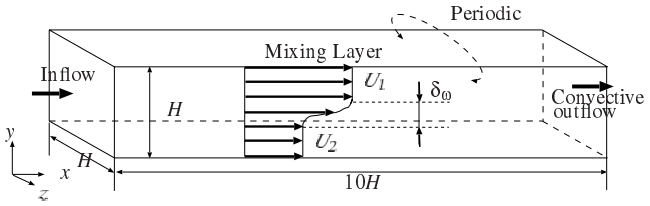

Figure 1: Overview of computational domain and boundary conditions.

The inflow condition consists of the mean velocity given by a hyperbolic-tangent profile, on which three-dimensional random perturbations are superposed:

$$u(0,y,z,t) = \frac{U_1+U_2}{2} + \frac{U_1-U_2}{2}\tanh\left(\frac{2y}{\delta_\omega}\right) + u'(y,z,t) \tag{6}$$

$$v(0,y,z,t) = v'(y,z,t) \tag{7}$$

$$w(0,y,z,t) = w'(y,z,t) \tag{8}$$

Here, the vorticity thickness δ_ω at the inlet is defined as follows:

$$\delta_\omega = \frac{\Delta U}{(dU(y)/dy)_{\max}} \tag{9}$$

where $U(y)$ is the mean velocity at the inlet. In this computation, δ_ω is set at $0.01H$. The velocity perturbation is given by uniform random numbers, and their amplitude is set at less than 1% of ΔU. At the outflow boundary, convective boundary condition without reflection as described in Okita and Kajishima [9] is used. In transverse, U_1 is given for the velocity at upper boundary, U_2 at lower boundary. Pressure boundary condition is set by Neumann boundary condition at the inflow and transverse

Table 1: Parameters for simulation

grid points	$N_x \times N_y \times N_z$	$800 \times 192 \times 120$
grid size	Δx	$1.25\delta_\omega$
	Δy	$0.521\delta_\omega$
	Δz	$0.833\delta_\omega$
Reynolds number	$Re(= H\Delta U/\nu_L)$	1×10^4
Mach number	M	0.1
time increment	Δt	$5 \times 10^{-5} H/\Delta U$
cavitaiton number	σ	$0.3, 0.4, 0.5,$ ∞ (non-cavitating)

boundary, and by Dirichlet condition at the outflow. Other parameters for this computation are shown in table 1. Four steps of cavitation number σ are dealt with: namely $0.3, 0.4, 0.5$ for cavitating condition, ∞ for non-cavitating condition (single phase). In cavitating condition, σ is set at ∞ in $x/H \leq 0.95$ to avoid cavitating in the roller-like vortices (as will hereinafter be described in detail). We adopt fully developed non-cavitating flow field as the initial condition.

OVERVIEW OF THE FLOW FIELD

In this section, we observe the flow field under non-cavitating and cavitating conditions. In following discussion, 'cavitation inception' region is assumed as the region where liquid volumetric fraction f_L is less than 1. Figure 2 represents the top and front view of instantaneous profiles of vortical structure and cavity at $T = 15$. Here, vortical structure is indicated by isosurface of second invariant of velocity gradient tensor Q colored by pressure value, and cavity by the isosurface of liquid volumetric fraction f_L. Figure 3 represents velocity vector expressed by advection frame under non-cavitating and cavitating condition. Velocity is based on the advection velocity $U = (U_1 + U_2)/2$. This figure shows that Q is corresponding to the vortical structure. In each figure of Fig. 2, very thin roller-like vortices are observed in the region $0 \leq x/H \leq 0.5$. These are caused by coarse grid; though the shear layer given as inflow boundary condition is very thin, the size of grid in streamwise direction isn't extremely fine because the flow in the vicinity of inflow is not important. Once these fluctuation disappear, they don't correlate with the mode observed in the process of development of turbulence in downstream. In cavitating condition, cavitation number σ is set at ∞ in $x/H \leq 0.95$ to avoid cavitating in the roller-like vortices. This computational setup doesn't affect the flow because thin roller-like vortices totally disappear in the region $x/H \geq 0.8$. Hereafter, we discuss the phenomena occurred in the region $1 \leq x/H \leq 10$.

Now we take a closer look at Fig. 2(a) to access the qualitative validity of non-cavitating condition. In the region $1.5 \leq x/H \leq 2$ ($x/H = 2$ at $T = 15$), we can observe primary roll-cell vortices generated due to Kelvin-Helmholtz instability. They are not so clear because of the threshold value of Q. K-H rollers are distorted by three dimensional perturbation and to be hairpin-like vortices. Secondary streamwise vortices (rib) are generated from developed hairpin-like vortices in $x/H \geq 3$. Secondary vortices are stretched in the streamwise direction between two K-H rollers (braid region). Figure 4 represents one of the typical streamwise vortex stretched between two roll-cell vortices. In the region $x/H \geq 2$, two rollers merge (pairing) due to velocity induced by each other, and become a larger one. As the result of pairing, the pitch of K-H rollers get longer in the downstream. This vortical structure is consistent with those in the previous experimental observation and theoretical studies of mixing layer.

In Fig. 2(b)-(d), cavity region is corresponding to the low-pressure area in the core of roll-cell vortices, hairpin-like vortices and also in the core of streamwise vortices. Cavity generated in roll-cell vortices and in streamwise vortices are partly merged and seem like cloud cavitation. Merging of cavity are caused mainly by advection and vortices pairing. Figure 5 shows the merging of cavity due to the pairing. In the downstream region, pitch of roll-cell vortices becomes longer than upstream region because of pairing. Figure 6 shows the time evolution of cavity area passing through $y - z$ cross sections. The graphs show that time interval of cavity passing tends to become longer in downstream region. Cavity collapses when low-pressure area in vortex core disappears. During the process of spatial development of mixing layer, a series of development of cavity are repeated: namely inception, growth, merge and collapse.

Under cavitating conditions, spatial position where roll-cell and hairpin-like vortices first appear shifts upstream compared with non-cavitating condition. The lower the cavitation number σ, the more upstream it shifts. At the lowest cavitation number $\sigma = 0.3$, the most upstream appearing position is $x/H = 1$, whereas $x/H = 1.5$ at non-cavitating condition. Besides, the position where vortices begin pairing also shift upstream. Cavity generation disturbs the flow field, so instability occurs more easily than non-cavitating condition. This is why vortices appearing position and pairing position shift upstream under the cavitating condition. In downstream region ($6 \leq x/H \leq 10$), pitch of roll-cell vortices tends to be longer and irregular at lower σ. As mentioned previously, cavity generation promotes pairing. This is related to longer pitch in downstream.

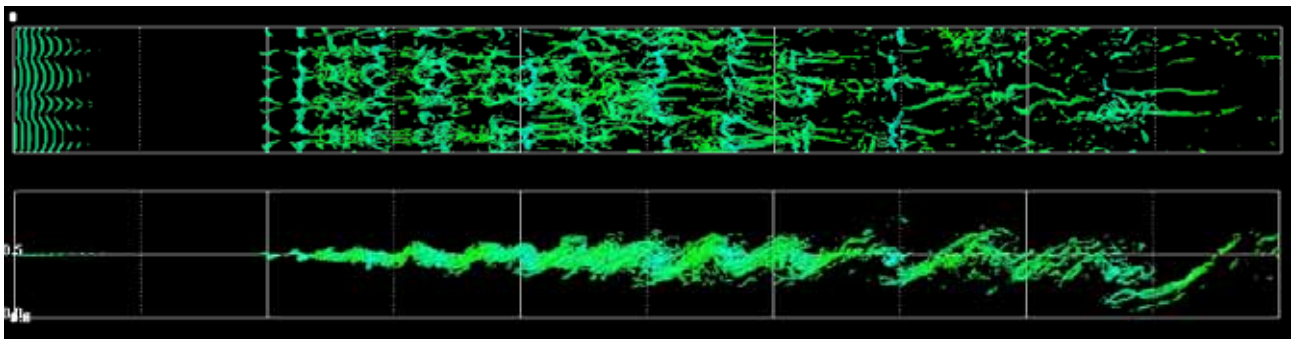

(a) Non-cavitating

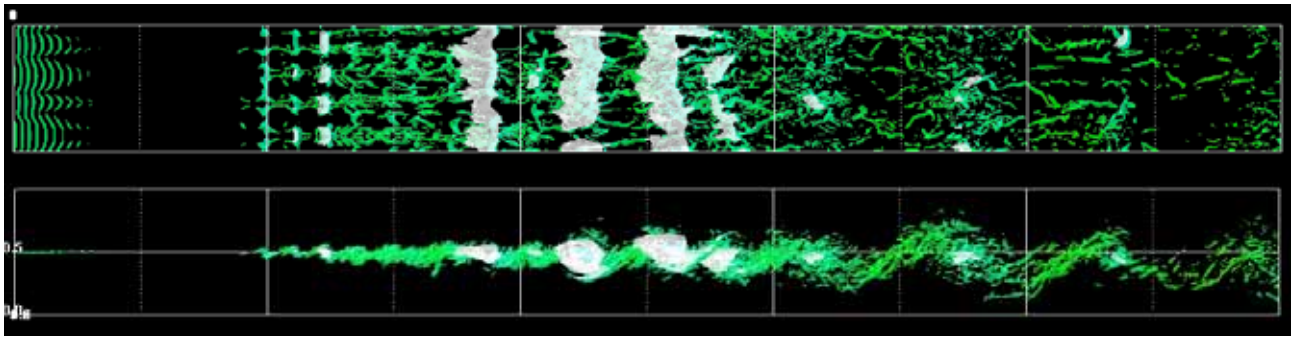

(b) $\sigma = 0.5$

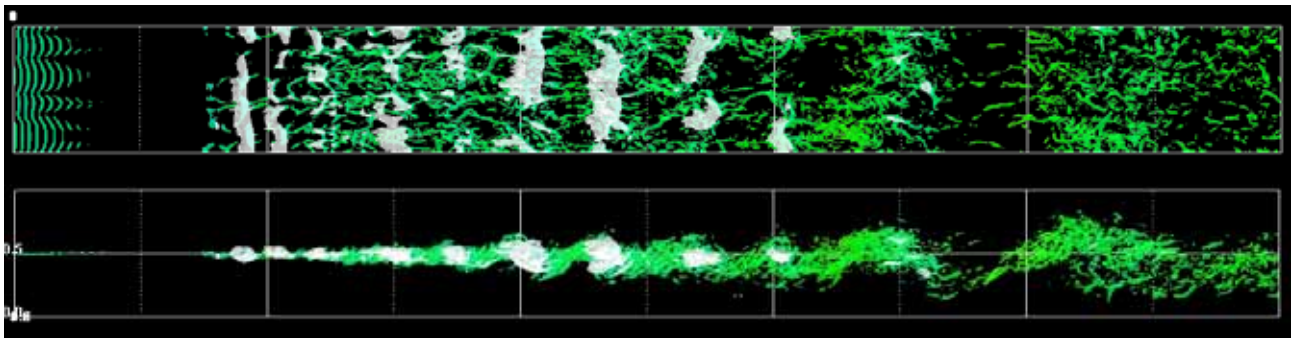

(c) $\sigma = 0.4$

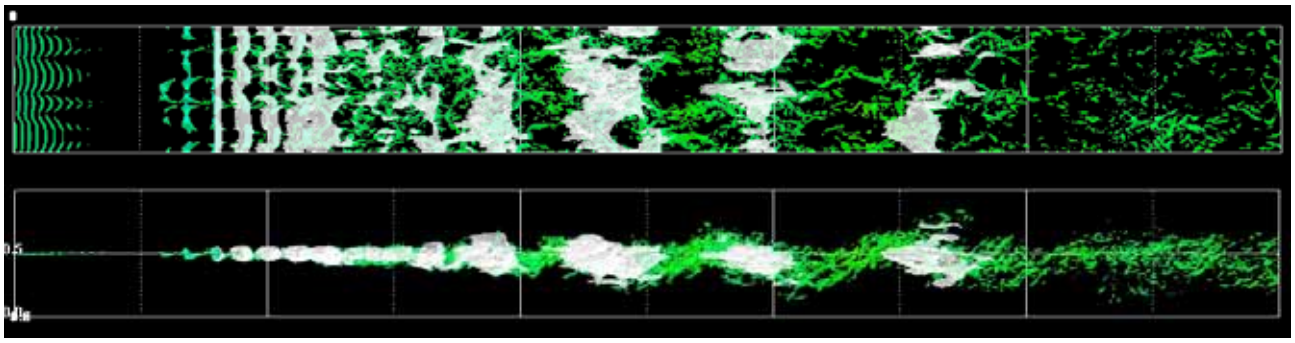

(d) $\sigma = 0.3$

Figure 2: Top and front view of instantaneous vortices and cavitation indicated by $Q = 230$ isosurface (colored to indicate the pressure value) and isosurface of $f_L = 0.999$ (white) at $T = 15$.

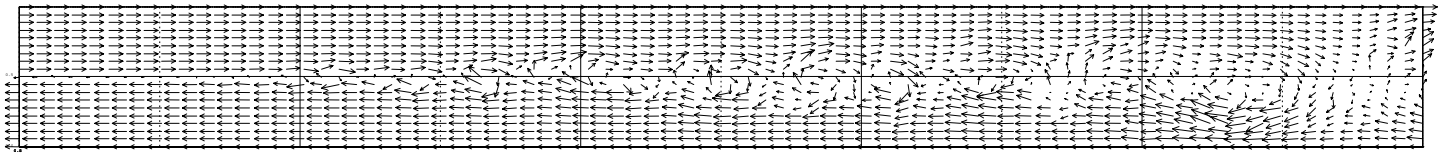

(a) Non-cavitating

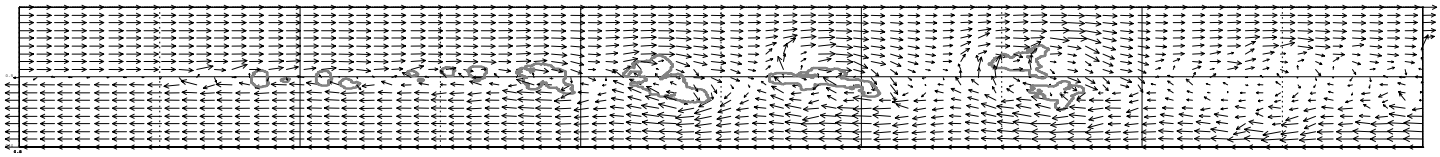

(b) $\sigma = 0.3$

Figure 3: Front view of instantaneous velocity vector and isoline of liquid volumetric fraction f_L (gray line).

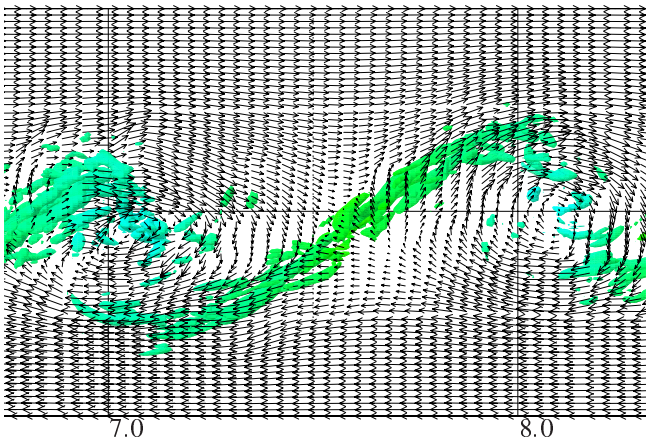

Figure 4: Streamwise vortex stretched between two roll-cell vortices.

MODIFICATION OF REYNOLDS STRESS BY CAVITATION

Here, we analyze these DNS database under cavitating and non-cavitating conditions to investigate the interaction between cavitation and turbulence. Figure 7 and 8 represent the distributions of normal components of Reynolds stress R_{22} and R_{33} along y-direction at three different cross-section in the flow field: (a) $x/H = 2$, (b) $x/H = 4$ and (c) $x/H = 8$, respectively. Reynolds stress R_{ij} is based on Favre average to consider the density fluctuation by cavitation.

$$R_{ij} = \bar{\rho}\widetilde{u_i''u_i''}/\Delta U^2 \tag{10}$$

In this computation, density of gas ρ_G is neglected and treated as void, so density of homogenous fluid ρ is represented as

$$\rho = \rho_G(1 - f_L) + \rho_L f_L \simeq \rho_L f_L. \tag{11}$$

Here, we assume that density fluctuation of liquid ρ_L' is sufficiently small for calculation of turbulence statistics, though we consider compressibility of liquid in this computation.

$$\rho_L f_L = (1 + \rho_L')f_L \simeq f_L \tag{12}$$

The value of Reynolds stress R_{ij} is therefore calculated as

$$R_{ij} = \overline{f_L}\widetilde{u_i''u_i''}/\Delta U^2. \tag{13}$$

Hereafter we compare all normal components and major component of shear R_{12}. In this paper, R_{22} and R_{33} are selected to show as representative examples of R_{ij}. Each cross-section represents following regions in the flow field, respectively:

(a) Streamwise vortices are developed and roll-cell vortices begin to merge.
(b) Most peak values of R_{ij} take maxima compared with other cross-section.
(c) Turbulence is fully developed and large scale merge of roll-cell vortices occurs.

From Fig. 7 and 8, we can observe that turbulence intensity is diffused from shear layer as turbulence is spatially developed. At $x/H = 2$, the lower the cavitation number, the smaller the R_{22} and R_{12} are. In the downstream region, on the other hand, tendency of R_{22} are completely opposite from the tendency in the upstream region.

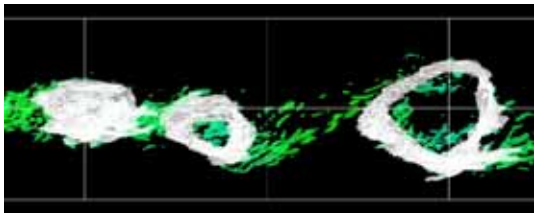

(a) $T = 2.8$

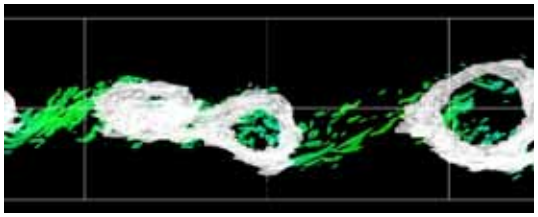

(b) $T = 3.0$

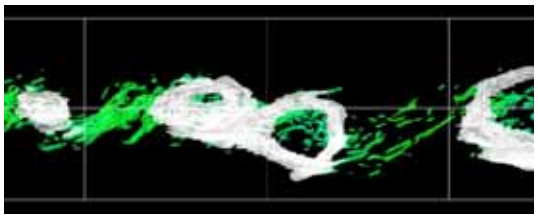

(c) $T = 3.2$

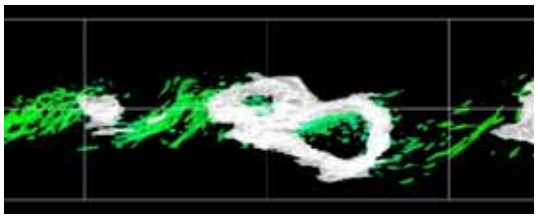

(d) $T = 3.4$

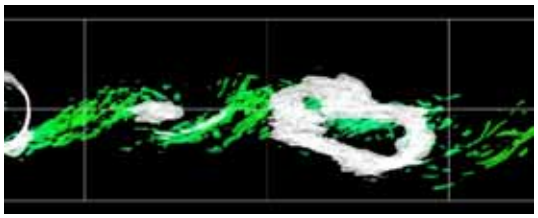

(e) $T = 3.6$

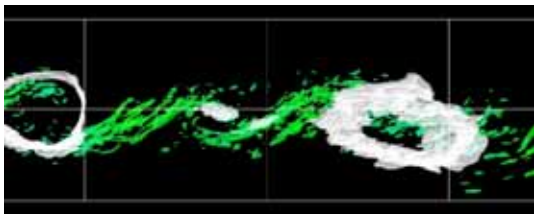

(f) $T = 3.8$

Figure 5: Merging of cavity by vortices pairing.

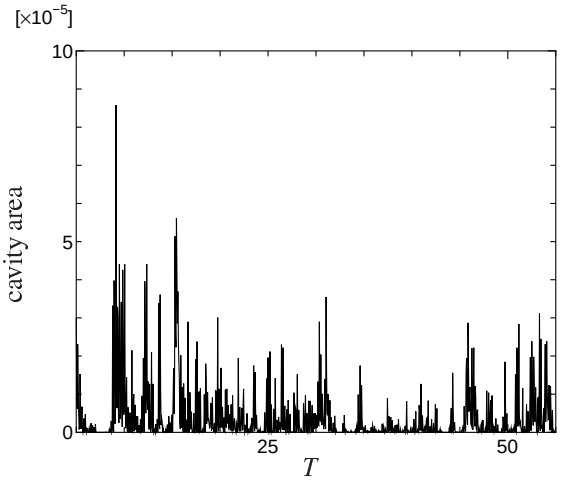

(a) $x/H = 2$

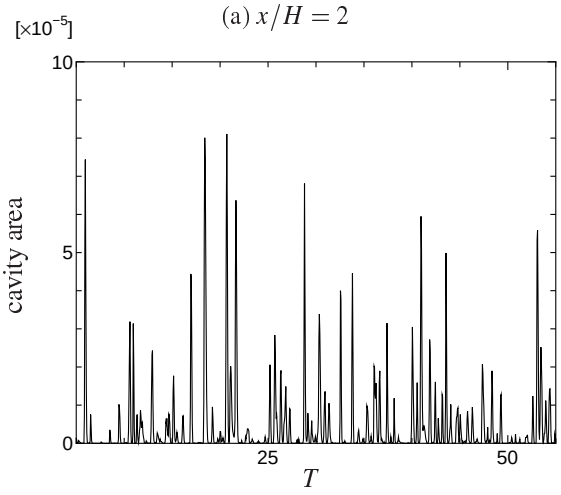

(b) $x/H = 4$

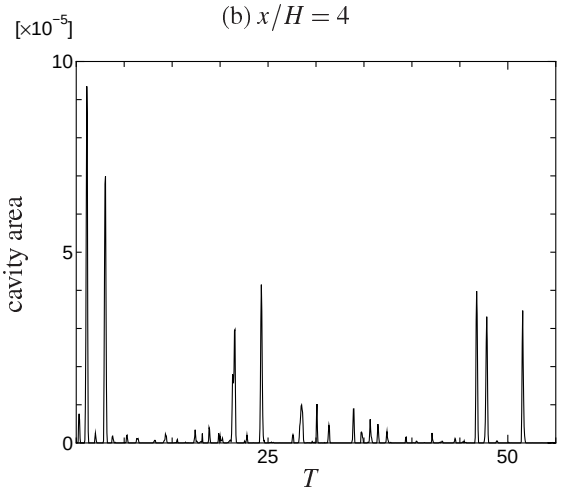

(c) $x/H = 8$

Figure 6: Time evolution of cavity area passing through three different $y - z$ cross sections ($\sigma = 0.3$, $5 \leq T \leq 55$).

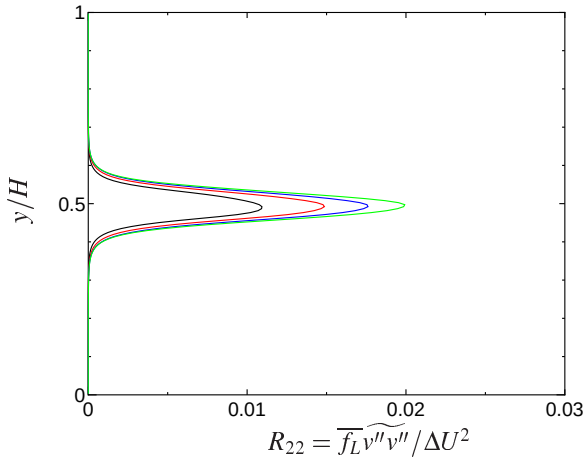

(a) $x/H = 2$

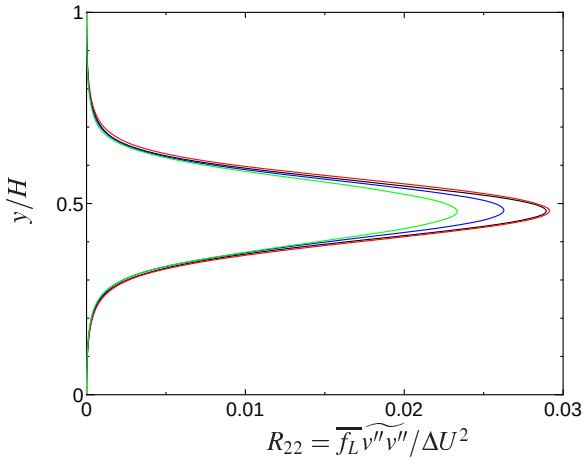

(b) $x/H = 4$

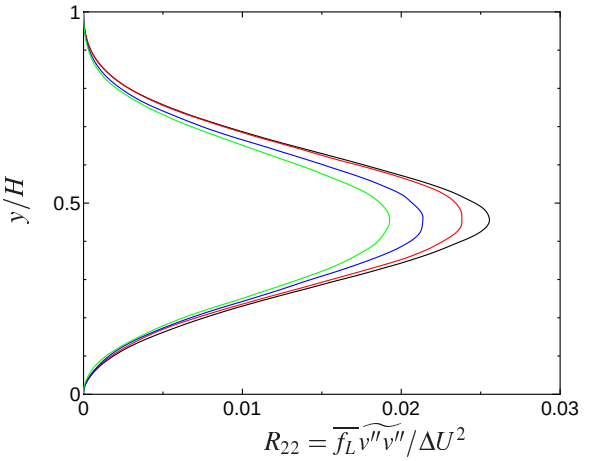

(c) $x/H = 8$

Figure 7: Modification of Reynolds stress R_{22} profiles by cavitation (black: non-cavitating, red: $\sigma = 0.5$, blue: $\sigma = 0.4$, green: $\sigma = 0.3$).

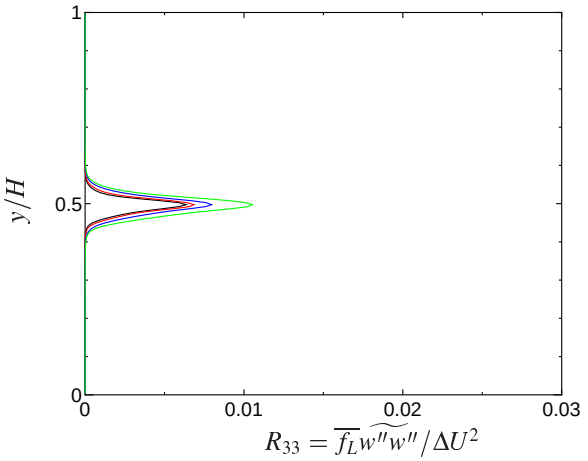

(a) $x/H = 2$

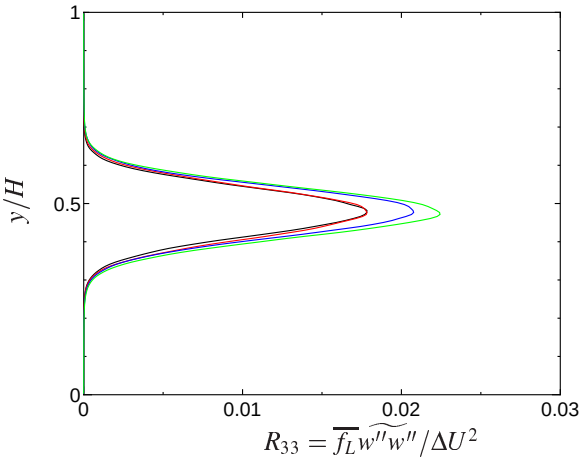

(b) $x/H = 4$

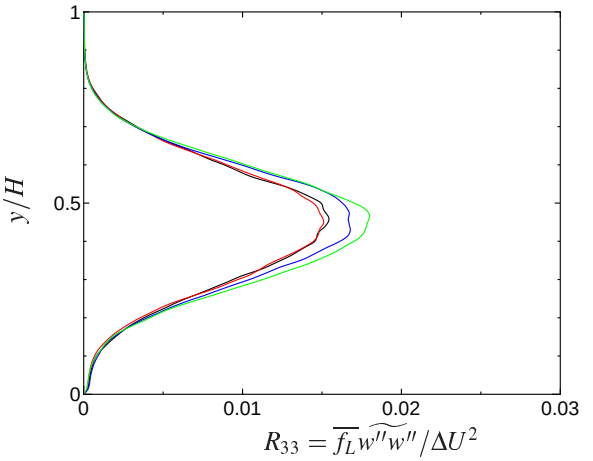

(c) $x/H = 8$

Figure 8: Modification of Reynolds stress R_{33} profiles by cavitation (black: non-cavitating, red: $\sigma = 0.5$, blue: $\sigma = 0.4$, green: $\sigma = 0.3$).

To discuss the difference of Reynolds stress between upstream and downstream, the peak value of normal and shear components of Reynolds stress in $y-z$ cross section are plotted along x-direction in Fig. 9. Each distribution has almost same tendency: In $1 \leq x/H \leq 4$, each component almost increases though there may be some inflection points. In $4 \leq x/H \leq 10$, each component decreases gently.

Upstream Region ($1 \leq x/H \leq 4$)

In the region $1 \leq x/H \leq 2$, spatial development of all components shift upstream at the lower σ. As mentioned before, instability occurs more easily under cavitating condition. This stimulates the development of roll-cell and streamwise vortices which is related to u'', v'' and w'' components. Development rate in $1 \leq x/H \leq 2$ of every component is almost same whereas position of spatial development changes.

Regardless of cavitation, R_{22} and R_{12} have some inflection points. In $2 \leq x/H \leq 3$, R_{22} and R_{12} take local maxima, and then decrease. This decreasing are caused by vortices pairing: time average v'' component decreases due to the decreasing of the number of roll-cell vortices. After the decline due to paring, R_{22} and R_{12} increase. In the region where some inflection points exist, R_{22} and R_{12} behave differently only at $\sigma = 0.3$, compared with other cavitating conditions. We guess that the difference of cavity generation between $\sigma = 0.3$ and other cavitating condition is related to these profile of R_{22} and R_{12}.

Figure 10 represents streamwise distribution of time-averaged cavity area in $y-z$ cross-section. This graph shows cavity area of $\sigma = 0.3$ is especially large compared with other cavitating conditions. This indicates cavity generation is not linear with respect to cavitation number.

R_{33} develops in the region $1 \leq x/H \leq 3$, and takes maximum at $3 \leq x/H \leq 4$. The region $1 \leq x/H \leq 3$ is transition region where hairpin-like vortices change into streamwise vortices, so the position where R_{33} takes the maximum is considered the completion point of transition.

Downstream Region ($4 \leq x/H \leq 10$)

In the upstream region ($1 \leq x/H \leq 4$), R_{22} and R_{12} increase after the decline due to paring. In the downstream region, vortices pairing are repeated and become large scale, so R_{22} and R_{12} tend to decrease. In Fig. 9(b), R_{22} is smaller at lower cavitation number. As mentioned previously, pitch of roll-cell vortices tends to be longer and irregular at lower σ: the merging of primary vortices seems to be promoted in the cavitation condition and the number of vortices are decreased. This is related to time average v'' component decreases. Besides, vortices are weakened by cavity expansion. When cavity expands in a vortex, the vortex is weakened. In our previous study, we conducted a DNS of cavitation in a single vortex, and confirmed that circumferential component of velocity and vorticity of the vortex is decreased by cavity expansion [12].

After taking minimum in $3 \leq x/H \leq 4$, R_{33} attenuates gradually in the downstream region. Under the cavitating condition, R_{33} tends to increase in comparison with non-cavitating condition. This is because cavity in streamwise or cloud-like cavity occur volume fluctuation. As mentioned previously, vortices are weakened by cavity expansion. Streamwise vortices are also weakened, so this effect may decrease w'' component. As for R_{33}, however, increasing of volume fluctuation by cavity is dominant. As for R_{22}, on the other hand, the suppression of v'' component is dominant rather than volume fluctuation.

CONCLUSION

The interaction between cavitation and turbulence is investigated by DNS of mixing layer under cavitating and non-cavitating conditions. In the cavitating condition, following tendencies are observed:

1. The position where roll-cell vortices first appear shifts upstream. Also, the position where vortices begin to merge (pairing) shifts upstream. Cavity generation disturbs the flow field, so instability occurs more easily than non-cavitating condition. Spatial development of Reynolds stress components also shift upstream.
2. Cavity generation is not linearly increased with respect to cavitation number. Therefore, tendency of turbulence modulation under especially low cavitation number is different from those at higher cavitation number.
3. Pitch of roll-cell vortices tends to be longer and irregular. Cavity generation seems to promote vortices pairing. This is why pitch of roller changes. R_{22}, which is corresponding to one of the circumferential components of roll-cell vortices, also changes: decreasing of the number of vortices causes suppression of v'' component, which is one of circumferential component of roll-cell vortices.
4. Weakened vortices by cavity expansion also result in decreasing of R_{22}.
5. R_{33} tends to increase in comparison with non-cavitating condition. This is because cavity in streamwise or cloud-like cavity occur volume fluctuation. As for R_{33}, increasing of volume fluctuation by cavity is dominant rather than suppression of w'' by weakened streamwise vortices.

As mentioned above, we could observe that a typical free turbulence is modulated by cavitation. We will propose a cavitation LES model which is based on One-equation dynamic model [13]. In One-equation dynamic model, turbulent energy K_{SGS} transport equation is dealt with to obtain the eddy-viscosity dynamically. This enables us to introduce the cavitation effect to the SGS flow field as the source term of K_{SGS} transport equation. We must consider two-way interaction when formulating the source term: namely, the prediction of cavitation inception

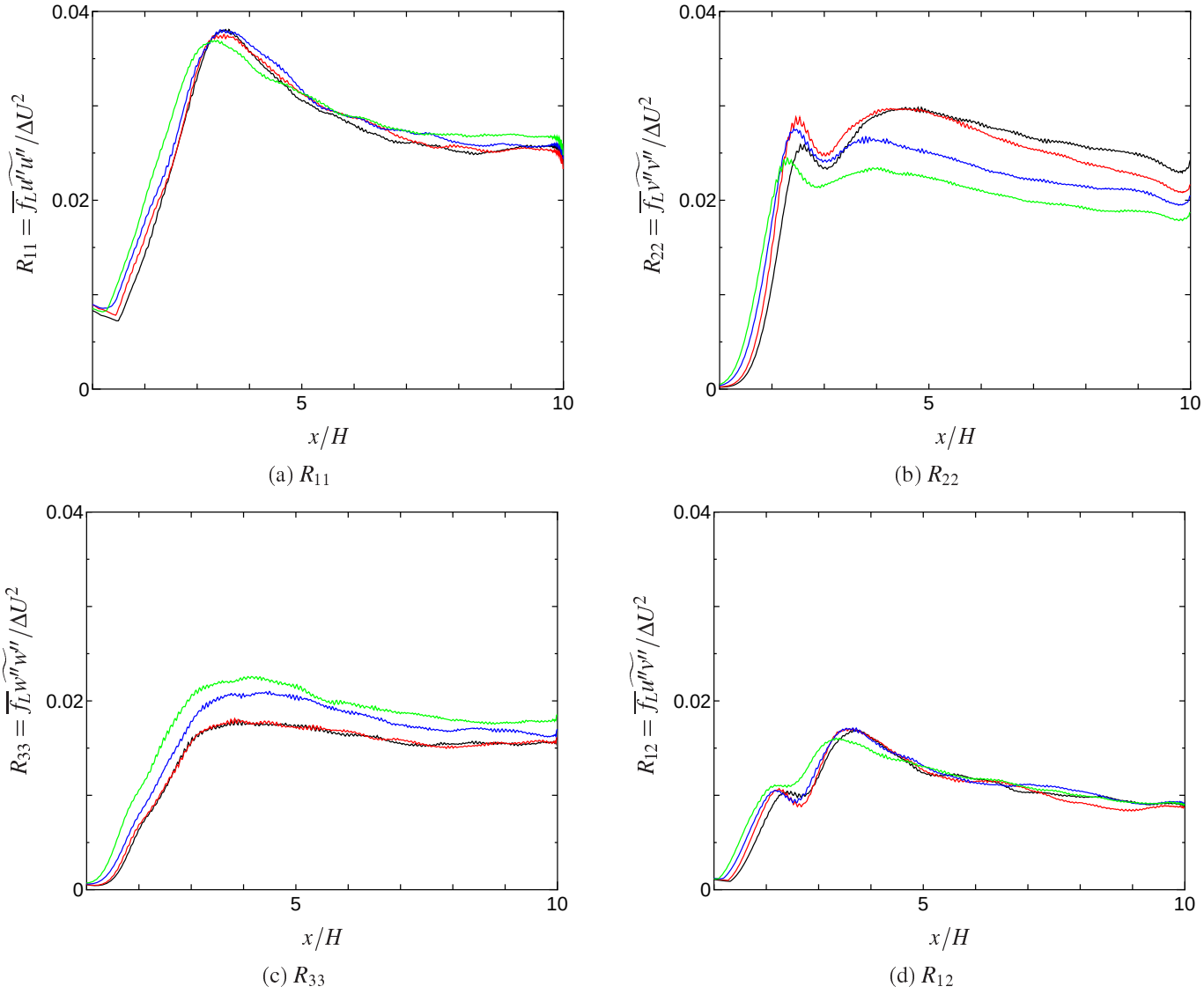

(a) R_{11} (b) R_{22}

(c) R_{33} (d) R_{12}

Figure 9: Distribution of peak value of Reynolds stress in streamwise direction (black: non-cavitating, red: $\sigma = 0.5$, blue: $\sigma = 0.4$, green: $\sigma = 0.3$).

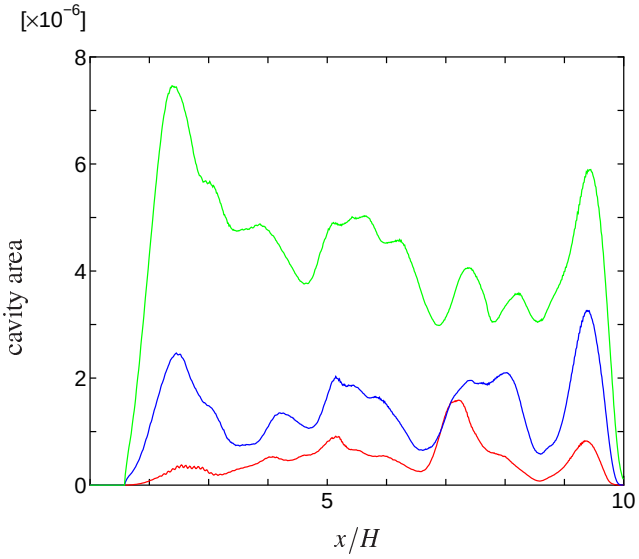

Figure 10: Streamwise distribution of time-averaged cavity area passing through $y-z$ cross sections (red: $\sigma = 0.5$, blue: $\sigma = 0.4$, green: $\sigma = 0.3$).

due to the SGS vortices and the source of turbulence energy due to the cavitation. In the present study, the latter part has been particularly highlighted. The flow around the cavitating vortex has been captured by our previous work [12] and it is used for the extra term in K_{SGS} equation. Then this concept will be evaluated in a priori manner by filtering the DNS database.

ACKNOWLEDGMENT

The authors express their gratitude to the contribution of Dr. Takashi Ohta. This study was supported by the Grant-in-Aid for Scientific Research of the Ministry of Education, Culture, Sports, Science and Technology - Japan. It was also partly supported by a collaborative research project with IHI Co.

NOMENCLATURE

c	sound speed
C_g	cavitation model constant
C_l	cavitation model constant
f_L	liquid volumetric fraction
H	height of computational domaint
M	Mach number
p	pressure
p_v	vapor pressure
Q	second invariant of velocity gradient tensor
Re	Reynolds number
R_{ij}	Reynolds stress component
T	Non-dimensional time
U	advection velocity
U_1	larger mean velocity
U_2	smaller mean velocity
u	velocity in mainstream direction
v	velocity in vertical direction
w	velocity in spanwise direction
x	coordinate in mainstream direction
y	coordinate in vertical direction
z	coordinate in spanwise direction

(Greek letters)

δ_ω	vorticity thickness
Δt	time increment for computation
ΔU	mean velocity difference
Δx	spacing of grid points in mainstream direction
Δy	spacing of grid points in vertical direction
Δz	spacing of grid points in spanwise direction
ρ	density of homogenous fluid
ρ_G	density of liquid
ρ_L	density of gas
σ	cavitation number

(Subscripts)

i	i-direction
∞	sufficient far position
$\bar{}$	Reynolds average
$\tilde{}$	Favre average
$'$	fluctuation from Reynolds average
$''$	fluctuation from Favre average

REFERENCES

[1] Coutier-Delgosha, O. et al., 2003, "Numerical Simulation of the Unsteady Behaviour of Cavitating Flows," *Int. J. Numer. Meth. Fluids*, Vol. 42, pp. 527-548.

[2] Kunz, R. F. et al., 2000, "A Preconditioned Navier-Stokes Method for Two-phase Flows with Application to Cavitation Prediction," *Computer & Fluids*, Vol. 29, pp. 849-875.

[3] Senocak, I. and Shyy, W., 2002, "A Pressure-based Method for Turbulent Cavitating Flow Computations," *J. Comp. Phys.*, Vol. 176, pp. 363-383.

[4] Ugajin, H. et al., 2006, "Numerical Simulation of Unsteady Cavitating Flow in a Turbopump Inducer," *Proc. of 42nd AIAA/ASME/SAE/ASEE Joint Propulsion Conference*, CD-ROM, AIAA2006-5068.

[5] Wang, G. and Ostoja-Starzewski, M., 2007, "Large Eddy Simulation of a Sheet/cloud Cavitation on a NACA0015 Hydrofoil," *Appl. Mathematical Modeling*, Vol. 31-3, pp. 417-447.

[6] Wienken, W. et al., 2006, "A Method to Predict Cavitation Inception Using Large-Eddy Simulation and Its Application to the Flow past a Square Cylinder," *J. Fluids Eng.*, Vol. 128-2, pp. 316-325.

[7] Yamanishi, N. et al., 2007, "LES Simulation of Backflow Vortex Structure at the Inlet of an Inducer," *Trans. of the ASME, J. Fluids Eng.*, Vol. 129-5, pp. 587-594.

[8] Arndt, R. E. A., 2002, "Cavitation in Vortical Flows," *Annu. Rev. Fluid Mech.*, Vol. 34, pp. 143-175.

[9] Okita, K. and Kajishima, T., 2002, "Three-dimensional Computation of Unsteady Cavitating Flow in a Cascade," *Proc. 9th International Symposium on Transport Phenomena and Dynamic of Rotating Machinery*, CD-ROM, No.FD-ABS-076.

[10] Inagaki, M. et al., 2000, "Numerical Prediction of Fluid-Resonant Oscillations at Low Mach Number," *Trans. of the Japan Society of Mech. Eng. Series B*, Vol. 66-649, pp,2274-2281 (in Japanese).

[11] Chen, Y., and Heister, S., 1995, "Two-phase Modeling of Cavitated Flows," *Computer & Fluids*, Vol. 24-7, pp. 799-809.

[12] Kajishima, T., Ohta, T., Sakai, H. and Okabayashi, K., 2007, "Influence of Cavitation on Turbulent Separated Flow," *Proc. 5th International Symposium on Turbulence and Shear Flow Phenomena (TSFP5)*, CD-ROM.

[13] Kajishima, T. and Nomachi, T., 2003, "One-equation Subgrid Scale Model Using Dynamic Procedure for the Energy Production," *ASME FEDSM2003*, CD-ROM, No. 45348.